



Aqueous phase conversion of CO₂ into acetic acid over thermally transformed MIL-88B catalyst

Received: 28 October 2021

Accepted: 5 May 2023

Published online: 17 May 2023

Check for updates

Waqar Ahmad¹, Paramita Koley¹, Swarit Dwivedi^{1,2}, Rajan Lakshman¹, Yun Kyung Shin², Adri C. T. van Duin², Abhijit Shrotri³ & Akshat Tanksale¹✉

Sustainable production of acetic acid is a high priority due to its high global manufacturing capacity and numerous applications. Currently, it is predominantly synthesized via carbonylation of methanol, in which both the reactants are fossil-derived. Carbon dioxide transformation into acetic acid is highly desirable to achieve net zero carbon emissions, but significant challenges remain to achieve this efficiently. Herein, we report a heterogeneous catalyst, thermally transformed MIL-88B with Fe⁰ and Fe₃O₄ dual active sites, for highly selective acetic acid formation via methanol hydrocarboxylation. ReaxFF molecular simulation, and X-ray characterisation results show a thermally transformed MIL-88B catalyst consisting of highly dispersed Fe⁰/Fe(II)-oxide nanoparticles in a carbonaceous matrix. This efficient catalyst showed a high acetic acid yield (590.1 mmol/g_{cat}.L) with 81.7% selectivity at 150 °C in the aqueous phase using Lil as a co-catalyst. Here we present a plausible reaction pathway for acetic acid formation reaction via a formic acid intermediate. No significant difference in acetic acid yield and selectivity were noticed during the catalyst recycling study up to five cycles. This work is scalable and industrially relevant for carbon dioxide utilisation to reduce carbon emissions, especially when green methanol and green hydrogen are readily available in future.

Fixation of overabundant atmospheric carbon dioxide is an urgent and essential research area that may lead to climate change mitigation. In 2019, carbon dioxide concentration reached 414.7 ppm, and it is anticipated that it may reach up to 500 ppm in 2050¹. Therefore, recycling of captured CO₂ into value-added products is desirable to avoid the catastrophic consequences climate change caused by CO₂ in the atmosphere². Several routes for carbon dioxide conversion have been investigated, but the thermocatalytic CO₂ hydrogenation pathway is extremely promising due to its fast kinetics, high productivity, scalability, and selectivity³. Synthesis of chemicals such as methane^{4,5}, methanol⁶, formaldehyde^{7,8}, dimethyl ether⁹, gasoline-range hydrocarbons¹⁰, oxymethylene dimethyl ethers^{11,12}, methyl formate¹³,

formic acid^{14,15}, and acetic acid^{16,17} have been investigated in recent years. A CO₂-based chemicals industry has the potential to lower the CO₂ concentration in the atmosphere while simultaneously providing revenue for offsetting the capture costs. The production of acetic acid (AA) via CO₂ hydrogenation is one such route that has recently received attention from researchers.

Acetic acid is extensively used in several industrial applications, including food, chemicals, pharmaceuticals, textile, cosmetics, and polymers¹⁸. Moreover, it is consumed in the synthesis of vinyl acetate monomer¹⁹, acetic anhydride²⁰, and cellulose acetate²¹. AA is also used as a solvent during terephthalic acid manufacturing^{22,23}. It is a well-known food preservative and is traditionally named vinegar in the food

¹Department of Chemical and Biological Engineering, Monash University, Clayton 3800, Australia. ²Department of Mechanical Engineering, The Pennsylvania State University, University Park, PA, USA. ³Institute for Catalysis, Hokkaido University, Sapporo 001-0021, Japan. ✉e-mail: akshat.tanksale@monash.edu

industry. Commercially, two major production processes are used for the synthesis of acetic acid – chemical and fermentative^{18,24}. Among various chemical routes, the most common industrial AA synthesis method is carbonylation of methanol (MeOH), where AA is produced through different processes such as BASF, Cativa, and Monsanto in the presence of homogeneous Cobalt, Iridium, and Rhodium catalysts, respectively. In the Monsanto process, AA is produced from CH₃OH and fossil fuel-derived CO in the presence of CH₃I and homogeneous rhodium-based catalyst^{16,18,25}. The main reaction of acetic acid production from methanol and CO is summarized in Eq. 1.

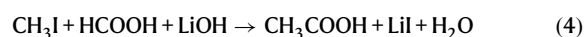
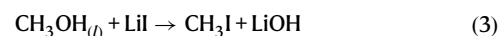


Gas phase CO₂ hydrogenation to AA, PA (propionic acid), and negligible amounts of C₄ acids (butyric acid and valeric acid), and other hydrocarbons (CH₄ and C₂–C₄) has been investigated using intermetallic Ni–Zn catalysts²⁶. Authors highlighted 13.4% CO₂ conversion with 58.9% and 18.2% selectivity for AA and PA, respectively, over Ni₃Zn–900 catalyst at 325 °C, 5400 mL.g⁻¹.h⁻¹ gas hourly space velocity (GHSV), 30 bar pressure, and H₂/CO₂ ratio 0.5²⁶. Qian et al. reported AA production via hydrocarboxylation of MeOH with carbon dioxide and hydrogen in 1,3-dimethyl-2-imidazolidinone (DMI) solvent over homogeneous Rh and Ru based homogeneous co-catalysts with a combination of Lil promoter and imidazole ligand. The stability of catalyst was dependent on the imidazole ligand. While the authors also report that imidazole played critical role in inhibiting the reverse water gas shift reaction, but the exact role of imidazole in the reaction mechanism was not clear¹⁶. The same group also showed AA synthesis via the above-described reaction system in the presence of Rh₂(CO)₄Cl₂ homogeneous catalyst, LiCl as a co-catalyst, 4-methyl imidazole ligand and Lil as a promoter²⁷. This reaction system is highly complex due to the presence of multiple catalysts, stabilizing ligands and organic solvents. In many cases, the authors report a black precipitate, which is not explained but is likely to be the Ru or Rh catalyst, which demonstrates that the system is not stable in these reaction conditions. However, the authors also demonstrated stable catalytic activity of Rh and Ru based homogeneous catalysts for five cycle during AA synthesis via methanol hydrocarboxylation reaction by using Imidazole ligand and Lil promoter in DMI solvent¹⁶. Hasan et al. reported low yield of AA (1.58 mmol/L) over NiO-C/Al₂O₃, heterogeneous catalyst at 130 °C and 35 bar total pressure of CO₂ and H₂ in 1,4 dioxane solvent after 6 h of reaction. Instead a higher amount of formic acid (FA, 4.08 mmol/L) was generated²⁸. Therefore, there is an urgent need to develop a stable and active heterogeneous catalyst based on low cost metals for AA synthesis which can be efficient for industrialisation and scaleup.

He et al. report FA and AA production via hydrothermal CO₂ reduction with Fe nanoparticles as stoichiometric reagent in which they are converted into ferrous carbonate²⁹. In 2021, Wang et al. described the acetate production from direct hydrothermal CO₂ hydrogenation in the vicinity of hexagonal closed packed cobalt (HCP-Co) catalyst and NaOH additive. The presence of CoO/Co interface was responsible for CO₂ activation followed by C–C coupling. A maximum of 9.5% acetate yield was achieved with HCP-Co after 6 h at 300 °C, 0.5 M NaOH, 40% water filling, and 40 mmol Co under 15 bar CO₂ and 35 bar H₂ atmosphere (optimized reaction conditions). The reaction pathway was dominated by [•]CH₂ and HCOO intermediates during CH₃COO⁻ formation via carbene reaction. Whereas, [•]CH₂ intermediate appeared from CO hydrogenation reaction³⁰. Recently, Yatabe et al. reported a plausible reaction mechanism of AA production through aqueous phase CO₂ hydrogenation with CH₃I additive over Rh-based homogeneous water-soluble catalyst, where, it plays the key role as electron storage catalyst. The water solvent is not only used as a green solvent but it also behaves as Lewis base by extracting H⁺ from hydrogen. In this study, AA turnover number (TON) was very low

(TON=1) using Rh-based homogeneous catalyst in the presence of CH₃I, LiBr (Lewis acid) and mixture of H₂O/CH₃OH (1/1) solvent after 24 h reaction at pH 2.0, and 80 °C under 1.5 bar CO₂ and 8 bar H₂ atmosphere³¹. To the best of our knowledge, Fe-based heterogeneous catalysts have not been reported for CO₂ conversion in aqueous phase. Heterogeneous catalysts have advantages in scale-up, and compares favourably against homogeneous catalysts which require large downstream separation processes.

Here we present a Fe-based thermally transformed metal organic framework catalyst (MIL-88B) for hydrocarboxylation of MeOH to produced AA. Recently, metal organic framework (MOFs) derived carbonaceous materials have been reported for their remarkable catalytic properties^{32–34}. Thermal transformation of MOFs results in a carbonaceous material with embedded metal or metal-oxide nanoparticles³⁴. As these particles are embedded in the matrix of decomposed organic linkers, they show greater resistance to sintering at higher temperatures. Depending on the thermal treatment, the thermally transformed MOFs have features such as high surface area, porosity, and fine dispersion of metal nanoparticles that are desired in an ideal heterogeneous catalyst. Moreover, the porous carbon framework provides better mass transfer to enhance the reaction rate. In this work, thermally transformed MIL-88B, called T-MIL-88B, consisted of dual active sites—Fe⁰ and Fe₃O₄, accelerating the conversion of CO₂ into AA, compared with other Fe-based catalysts tested which contained only Fe₃O₄ or Fe⁰ and Fe₂O₃. In this process, AA is produced in a series of reactions^{15,16,25} (Eqs. 2–4)—



Overall Reaction



Results and discussion

Catalyst characterisation

Figure 1a–c illustrates the PXRD diffractograms of the catalysts, before and after catalytic tests. Calcined Fe/CBEA catalyst showed characteristic peaks of α-Fe₂O₃, most of which were not observed in the reduced catalyst. Instead, the reduced catalyst showed Fe⁰ peaks at 2θ = 44.7° and 65° and residual α-Fe₂O₃ peaks at 35.98° and 62.83°. However, there were no Fe⁰ or α-Fe₂O₃ peaks detected in the used catalyst which indicated leaching of Fe from the catalyst support. The residual reaction solution slowly turned to red color over a period of few days, indicating presence of iron oxides in the solution. Therefore, Fe/CBEA catalyst was not considered further.

Both the fresh and the used T-Fe/MIL-101 catalyst showed peaks corresponding to Fe₃O₄, suggesting that the catalyst was stable after the reaction. However, the α-Fe₂O₃ peaks observed in Fe/MIL-101 (Fig. S1a, ESI) which did not reduce to Fe⁰ in T-Fe/MIL-101.

Figure S1b shows the PXRD pattern of MIL-88B which has good resemblance with literature^{35,36}. Characteristic peaks of T-MIL-88B-495, T-MIL-88B-500 and T-MIL-88B-505 catalysts revealed the transition in iron phases after thermal transformation of MIL-88B at different temperatures (Fig. S1c). Diffraction peaks of T-MIL-88B-495 show the presence of mainly Fe₃O₄ phases (Fig. S1c), whereas, T-MIL-88B-500 catalyst peaks showed both Fe₃O₄ and Fe⁰ (Fig. 2c and Fig. S1c), while, T-MIL-88B-505 presented major peaks of Fe₃C and Fe⁰, and few low-intensity peaks of Fe₃O₄ phases (Fig. S1c). These results suggested the

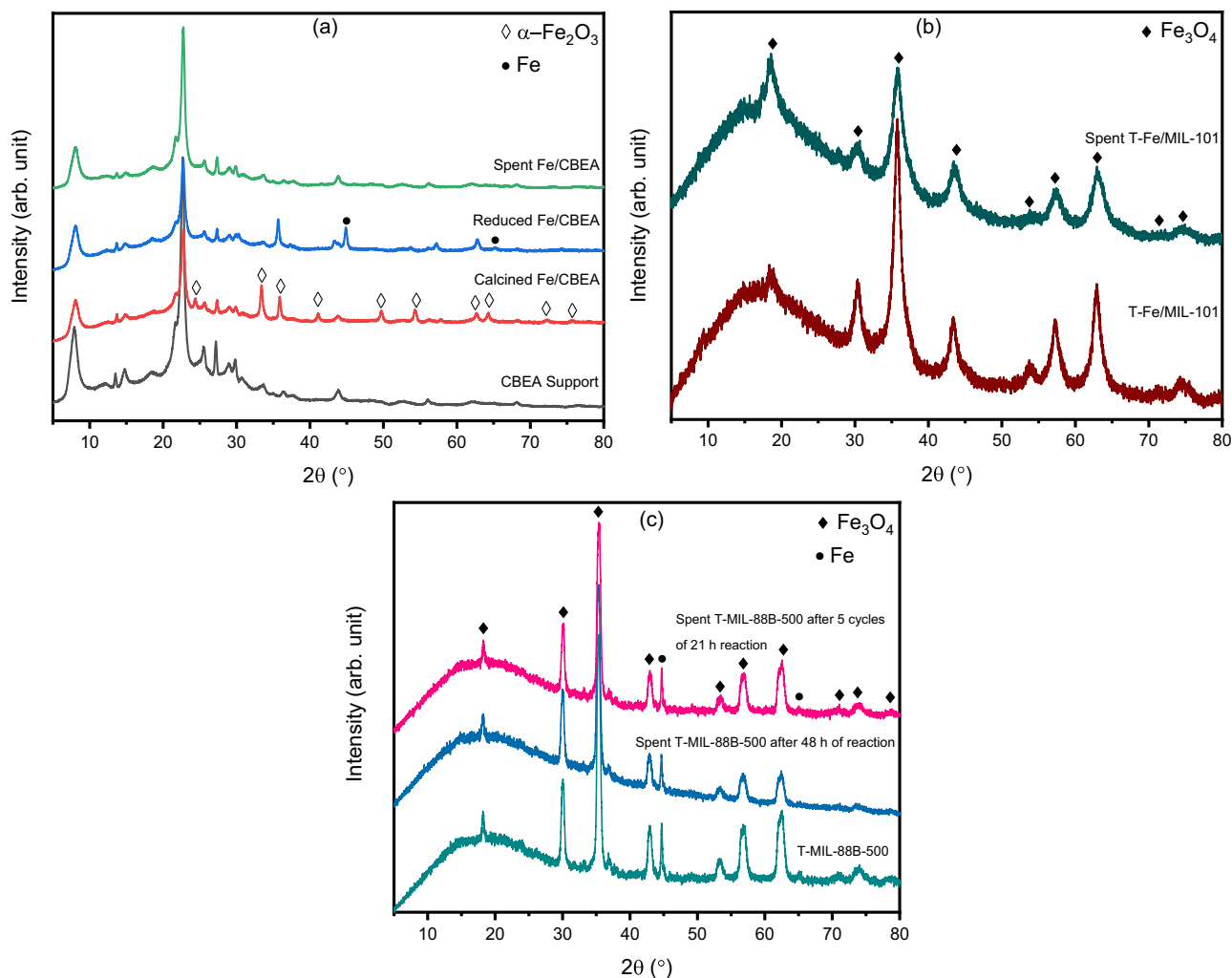


Fig. 1 | Powder X-Ray Diffraction (PXRD) patterns of the as synthesized and used catalysts used in this study. a as prepared, calcined, reduced and used Fe/CBEA, **b** as prepared and used T-Fe/MIL-101, and **c** as prepared and used T-MIL-88B

catalysts after 48 h reaction in presence of CH₃I and 5 cycles of 21 h each in presence of CH₃OH and LiI.

vital role of temperature during thermal transformation of MIL-88B under reducing atmosphere because a small change in temperature alters the structure of catalyst. Both Fe₃O₄ and Fe⁰ peaks of the T-MIL-88B-500 catalyst remained unchanged after a single run of 48 h reaction time and 5 cycles of 21 h each (Fig. 1c). Only Fe₃O₄ peaks have been reported after the thermal treatment of MIL-88B at 500 °C under nitrogen atmosphere³⁷. However, due to the reducing atmosphere used in this study, some of iron oxide nanoparticles reduced to Fe⁰ at 500 °C. No evidence of iron carbide was found in the PXRD results of T-MIL-88B-500.

During the thermal transformation of MOFs, first, the linkers break from the metal oxide clusters. After that, the metal oxide clusters agglomerate and reduce depending upon the chemical environment. Figure 2a shows the MIL-88B structure consisting of the Fe₃O clusters coordinated by six carboxylate ligands and three adsorbed water molecules. The ligands can be water, hydroxylate, or fluorine depending on the synthesis method. Upon heating the MOF, we observe an increase in the density, characteristic of the negative thermal expansion coefficient of the MOF (Fig. 2b). The behaviour is similar to our earlier study of thermal transformations in Zr-based MOFs³⁸. At approximately 500 °C, the linkers start detaching from the cluster, and the framework begins to collapse. Consequently, we observe a significant increase in the density of the system. After detachment of the organic linkers, the linkers go through thermolysis,

forming small gaseous molecules such as H₂, H₂O, CO, and CO₂. These molecules were periodically removed from the simulation box to mimic the gas and solid phase separation. The thermally transformed MOF cooled at 300 K is shown in Fig. 2c–e). The MOF treated at 1500 K for 200 ps shows a larger number of oxygenated molecules, mostly present as the carboxylate groups attached to the Fe atoms. However, upon treating the MOF at 2000 K for 500 ps, most of the carboxylate oxygen atoms are removed in the form of CO, CO₂, and H₂O, and a Fe-C_x matrix is dominant. On the other hand, upon treating the MOF at 1500 K for 500 ps, we observe the carboxylate oxygens partly removed in the form of small gasses, whereas the remaining oxygen atoms are present in the Fe-matrix.

We can better understand the local coordination of Fe atoms by plotting the radial pair distribution function (*g*(*r*)). Figure 3a shows the *g*(*r*) for the Fe-Fe pair. The characteristic peak of MOF (-3.8 Å) is diminished in all the thermally transformed MOFs, which indicates that the Fe₃O cluster arrangement is broken. The Fe-Fe peaks in the transformed MOFs are similar to the BCC/FCC phase of Fe. The two peaks between 2 Å and 3 Å in the Fe-BCC/FCC structure are merged into one peak in the thermally transformed MOFs, commonly observed in high-temperature quenching of iron³⁹. Similar behaviour is observed for the peaks between 4 Å and 6 Å. Figure 4b shows the *g*(*r*) for the Fe-O pair. All the thermally transformed MOFs have the highest peak at -1.5 Å representing the O/OH bonded to Fe atom. Although the

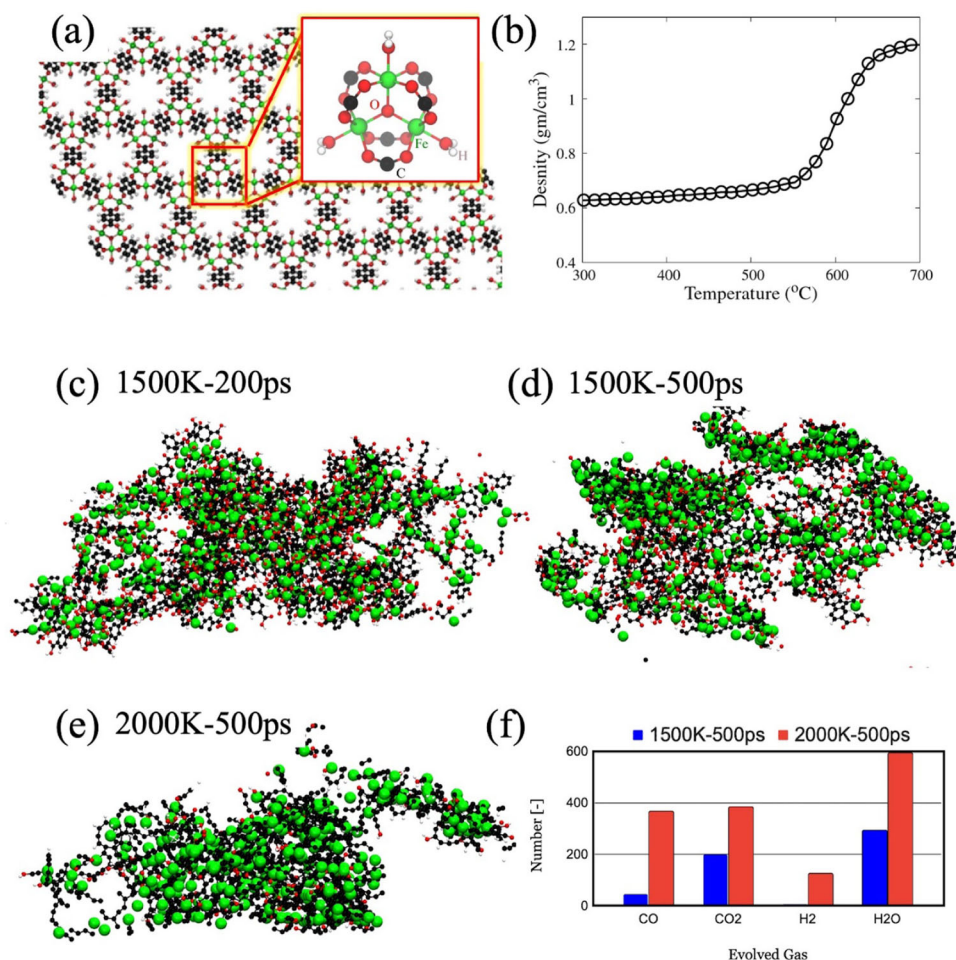


Fig. 2 | Thermal transformation of MIL-88B(Fe) structure. **a** Shows the MIL-88B (Fe) MOF and metal cluster topology in the inset and **b** shows the density change during heating. The final transformed structures cooled at 300 K after the thermal

treatment at **c** 1500 K for 200 ps, **d** 1500 K for 500 ps, and **e** 2000 K for 500 ps. **f** The total number of gas molecules removed evolved during the thermal treatment.

MOF treated at 2000 K has the largest peak, this is due to nearly all the remaining oxygen atoms being bonded to Fe atoms in form of O/OH. A peak around -1.9 \AA is observed, prominently for MOF transformed at 1500 K for 500 ps. This peak is similar to oxygen atoms present within the Fe-matrix, similar to the first peak of Fe_2O_3 and Fe_3O_4 . This peak is absent for the other two thermally transformed structures. Based on these results, we conclude that upon heating, first, the carboxylate oxygen is removed from the system, and Fe_3O clusters partly arrange in the form of $\text{Fe}_2\text{O}_3/\text{Fe}_3\text{O}_4$ clusters in a Fe and C matrix. However, the interstitial oxygen is removed upon further heating, and a Fe-nanoparticle/Fe-C matrix forms at 2000 K. Figure 3c shows the $g(r)$ for the Fe-C pair. A peak of Fe-C is observed at -2.4 \AA ; however, it does not match the Fe-C peak in Fe_3C at -2 \AA . Therefore, carbon is present in the iron matrix, not in the Fe_3C phase.

Figures 4a–f show the TEM images of MIL-101, Fe/MIL-101, T-Fe/MIL-101, MIL-88B, T-MIL-88B-500, and used T-MIL-88B-500, respectively. MIL-101 shows the characteristic octahedral shape of ca. 200–300 nm size (Fig. 3a and Fig. S6a, ESI)⁴⁰. After impregnation of Fe over MIL-101, agglomerates of Fe nanoparticles were observed on MIL-101 (Fe/MIL-101) with approximately 50–100 nm in size (Fig. 4b), whereas after thermal transformation, T-Fe/MIL-101 exhibited approximately 5–30 nm particles (Fig. 4c). The emergence of these smaller nanoparticles is likely due to the thermal transformation of Fe/MIL-101 in reducing atmosphere, where the deconstruction of linkers leads to breakage of the Fe agglomerates. Figure 4d and Fig. S6b (ESI) show the characteristic fusiform rod-shaped morphology of MIL-88B with

$\sim 360 \text{ nm}$ length and 90 nm width³⁷. After thermal transformation, T-MIL-88B-500 shows a narrow range of $\text{Fe}^0/\text{Fe}_3\text{O}_4$ nanoparticle which are well-dispersed over the carbonaceous support (Fig. 4e). The amount of Fe on T-MIL-88B-500 is 49.3%, with 13.7% C and negligible amount of H, N and S (Table S1, ESI), which indicates that original MOF structure is completely transformed into porous carbon. Moreover, CO pulse chemisorption results reveal 0.017% Fe metal dispersion for T-MIL-88B-500 with the metal surface area of $0.055 \text{ m}^2/\text{g}$. Figure 4f shows that the T-MIL-88B-500 catalyst retains its structure after 48 h of reaction. Figure 4g, h illustrates the particle size distribution (PSD) for T-MIL-88B-500 and used T-MIL-88B-500, respectively. 525 and 476 particles were measured from multiple images which showed most of the particles in 4–16 nm for both fresh and used T-MIL-88B-500, respectively. The peaks were observed at 8 nm with average particle sizes of 9.7 and 9.1 nm for fresh and used T-MIL-88B-500, respectively which suggested that T-MIL-88B-500 is stable and potentially reusable for this reaction.

The surface oxidation state of Fe in the different catalysts was evaluated by X-ray photoelectron spectroscopy (XPS), as shown in Fig. S2 (ESI). For T-MIL-88B-500 (Fig. S2a), Fe $2p_{3/2}$ XPS spectrum exhibited three peaks, including a peak at 706.7 eV corresponding to metallic iron⁴¹. Moreover, the other two peaks at 710.0 and 712.09 eV which are correlated to Fe^{+2} and Fe^{+3} oxidation state of iron and a satellite peak appeared at 719.07 eV⁴². In the Fe $2p$ region of T-MIL-88B-500, Fe $2p_{1/2}$ and Fe $2p_{3/2}$ peaks at 710.0 and 723.7 eV, respectively, having a spin-orbital splitting of 13.7 eV indicate the presence of Fe_3O_4

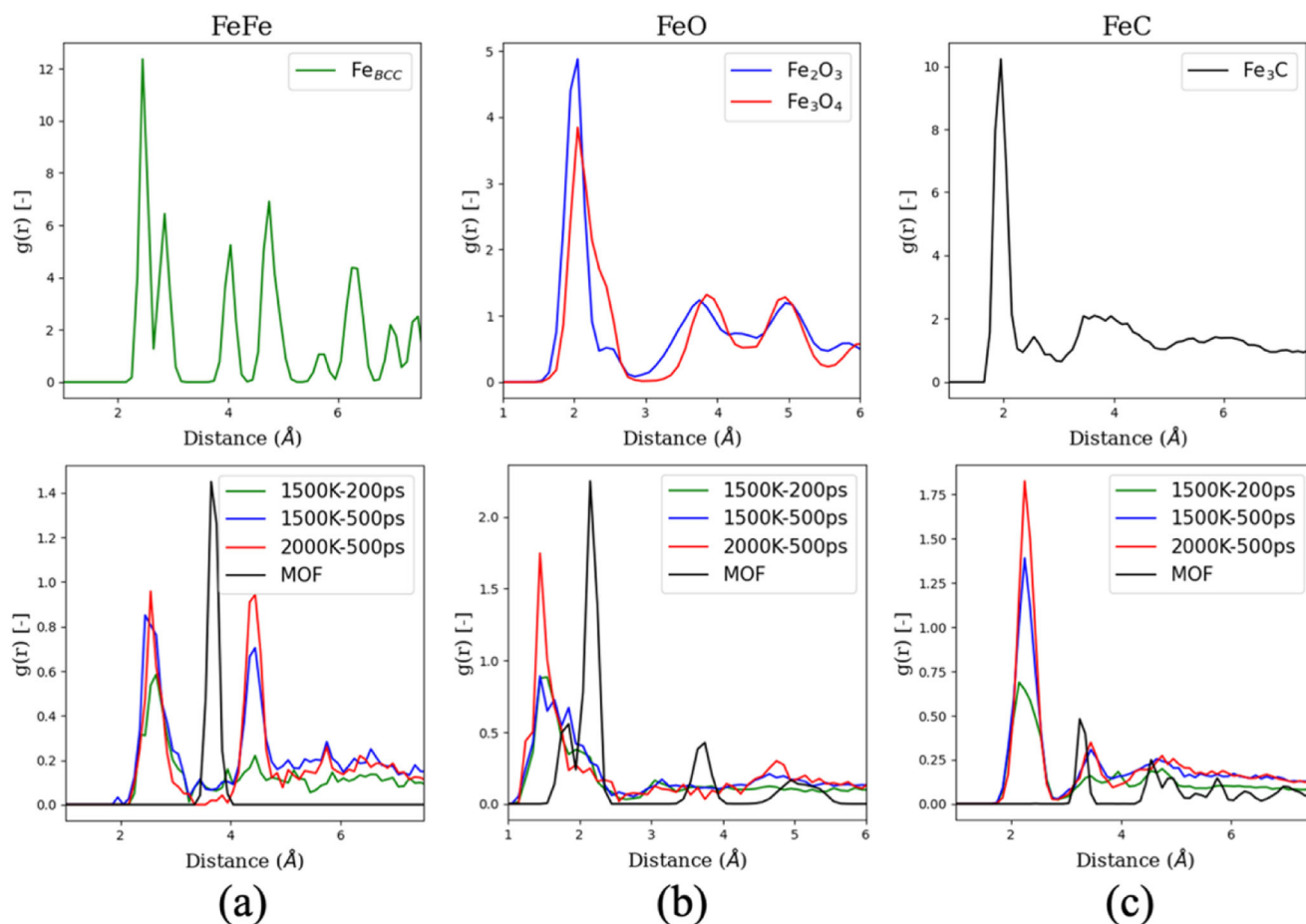


Fig. 3 | Radial pair distribution function of thermally transformed and parent MIL-88B metal organic framework (MOF). a Fe-Fe, b Fe-O, and c Fe-C pairs. The top graph shows the $g(r)$ for the reference materials whereas the bottom graph shows the $g(r)$ for MOF and the thermally transformed MOFs.

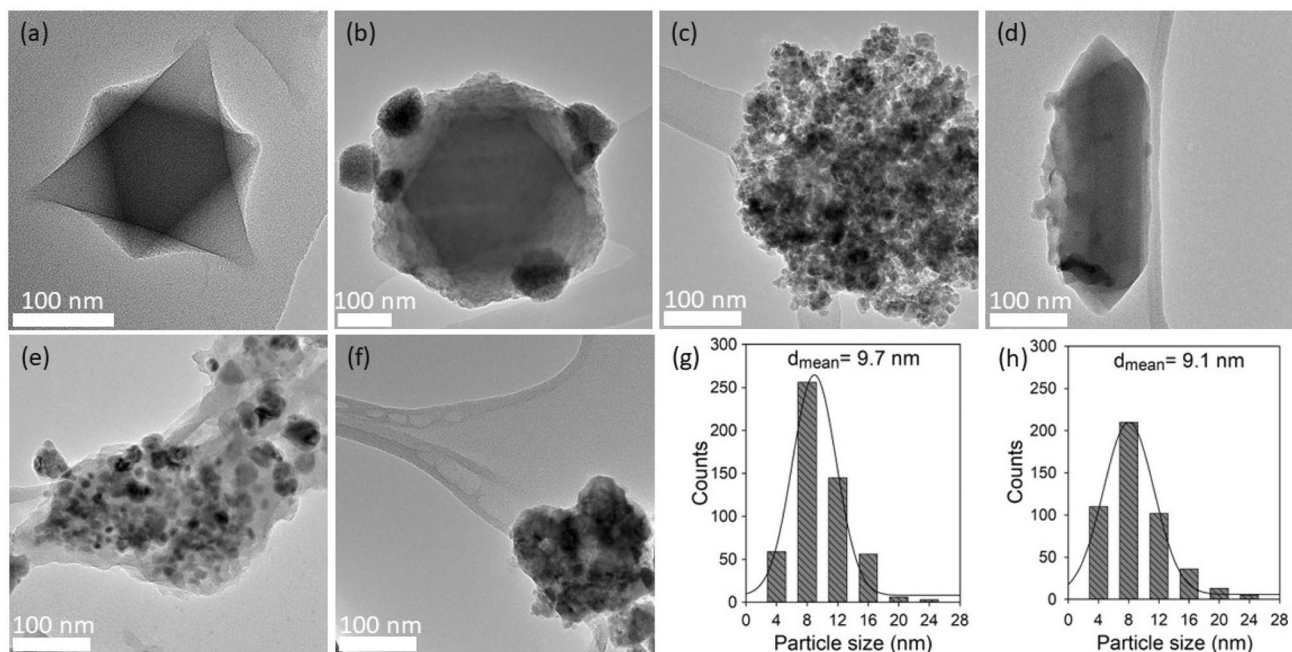


Fig. 4 | TEM micrographs of various catalysts used in this study. a MIL-101, b Fe/MIL-101, c T-Fe/MIL-101, d MIL-88B, e T-MIL-88B-500, and f used T-MIL-88B-500 after 48 h of aqueous phase CO_2 hydrogenation reaction in the vicinity of CH_3OH and LiI additives; and particle size distribution of g T-MIL-88B-500, and h used T-MIL-88B-500.

in T-MIL-88B-500⁴³. Fe₃O₄ may exist as mixed FeO and Fe₂O₃ states, which appears from Fe⁺² and Fe⁺³ oxidation states⁴⁴. The present XPS study shows that Fe₃O₄ is the dominant species on the surface, where the amount of Fe⁺² was 48.4% and Fe⁺³ was 34.5%, whereas Fe⁰ was 17.1%. Therefore, the ratio of Fe⁰ to Fe₃O₄ was accounted as 1:4.85 in T-MIL-88B-500.

The XPS spectra of Fe 2p_{3/2} in T-Fe/MIL-101 exhibited two peaks at 710.7 and 712.4 eV which is relate to Fe⁺² and Fe⁺³ along with satellite peak at 719.03 eV. Furthermore, Fe 2p_{1/2} and Fe 2p_{3/2} of Fe⁺² appeared at 710.7 and 724.4 eV and the spin-orbital splitting is 13.7 eV which is interpreted as Fe₃O₄ in T-Fe/MIL-101. Metallic Fe peak is absent in this catalyst which is in good agreement with PXRD results. For Fe/MIL-101 catalyst, Fe 2p_{3/2} XPS spectra also contained both Fe⁺² and Fe⁺³ at 710.6 and 712.3 eV, respectively. However, the spin-orbit splitting for Fe 2p_{1/2} and Fe 2p_{3/2} is 14.0 eV (724.6 and 726.5 eV) which suggested the absence of Fe₃O₄ phase. For MIL-88B, Fe 2p_{3/2} XPS spectra is included both Fe⁺² and Fe⁺³ peaks at 710.1 and 711.6 eV. Although, the spin-orbit coupling for Fe 2p_{1/2} and Fe 2p_{3/2} is 13.36 eV (723.57 and 725.3 eV) which confirmed that Fe₃O₄ is not present in MIL-88B. Figure S2b represent the Cr XPS spectra of MIL-101, Fe/MIL-101 and T-Fe/MIL-101 catalysts. In MIL-101, Cr 2p XPS spectra contained only one peak at 577.6 eV which corresponds to Cr⁺³ oxidation state⁴⁵. For Fe/MIL-101, Cr XPS spectra attributed to two peaks at 577.2 and 578.8 eV which mainly resembles with Cr⁺³ and CrO₃⁴⁶. The negative binding energy shift (0.4 eV) of Cr⁺³ as compared to Cr⁺³ present in MIL-101 is most likely due to the interfacial electronic interaction (charge transfer) between Cr and Fe after the inclusion of Fe in MIL-101⁴². The Cr spectra for T-Fe/MIL-101 mainly consisted Cr⁺³ peak at 577.1 eV and the amount of CrO₃ is very low as compared to Fe/MIL-101 which may be due to the thermal transformation of Fe/MIL-101 under hydrogen atmosphere that reduces the Cr oxides species on catalyst surface.

The C 1s XPS spectra for MIL-88B and Fe/MIL-101 (Fig. S2c) show three different types of C peak at 284.8, 285.6 and 289.0 eV which belongs to C–C, C–O–C and O–C=O, respectively⁴⁷. In the C 1s XPS spectra of T-Fe/MIL-101, the O–C=O peak intensity decreased as compared to MIL-88B and Fe/MIL-101. Moreover, the C 1s XPS spectra of T-MIL-88B-500 contains only two peaks corresponding to C–C and C–O–C, whereas, the O–C=O peak is absent, which is likely due to the evolution of CO and CO₂ during thermal transformation of both Fe/MIL-101 and MIL-88B, reducing the oxygen content in the catalyst.

Figure S3 (ESI) illustrates the XANES analysis of Fe L_{2,3}-edge in MIL-88B and thermally transformed MIL-88B at different temperatures and compared with reference Fe₂O₃. MIL-88B showed one major peak at 706 eV, with a shoulder at 708 eV for Fe 2p_{3/2}, where the high intensity 706 eV peak is most likely related with the Fe₃O coordinated iron complex⁴⁸. However, the emergence of shoulder peak highlighted the existence of higher oxidation state of iron in MIL-88B. Here, T-MIL-88B-495, T-MIL-88B-500 and T-MIL-88B-505 exhibited the high-intensity peak at 708 eV which is consistent with Fe₂O₃ peak. However, the shoulder at 706 eV observed in thermally transformed MIL-88B may be attributed to partially reduced iron oxide. T-MIL-88B-505 showed the most intense shoulder at 706 eV, which indicates higher degree of reduction of iron particles with increasing temperature during thermal treatment of MIL-88B.

A thermogravimetric analysis of Fe/MIL-101 and MIL-88B under Ar atmosphere is shown in Fig. S4a (ESI). For Fe/MIL-101, the weight loss in the range of 50–250 °C is because of the evaporation of water and removal of free terephthalates inside the pores of MOF⁴⁹. Thereafter, the main weight loss in the temperature range of 270 to 670 °C is due to the degradation of organic ligand in the framework of MOF which is attributed to the collapse of the framework⁴⁹. The weight loss of MIL-88B before 250 °C corresponds to the removal of water and excess DMF from the framework³⁶. Further weight loss in the temperature range of 300 to 500 °C is due to the degradation of H₂BDC and the breakdown of the framework. The step in the TGA profile of between

550–650 °C is most likely due to the carbonization of the framework and the formation of Fe₃O₄–carbon composites³⁶.

Figure S4b (ESI) compares TG and DTG analysis of MIL-88B under 5%H₂/N₂ and pure N₂ atmosphere. No significant difference in weight loss was observed below 400 °C for the two cases. However, the weight loss between 400–495 °C is higher and faster under the reducing atmosphere. In the 5%H₂/N₂ atmosphere, the higher intensity DTG peak at 450 °C is believed to be due to the reduction of Fe₃O₄–carbon composites, which is in good agreement with the PXRD of T-MIL-88B-495 (Fig. S1c) and published PXRD of MIL-88B treated at 500 °C under N₂ atmosphere³⁷. Moreover, an additional DTG peak emerged at 495–530 °C under 5%H₂/N₂ mixture which shows continuing reduction to form Fe⁰–carbon and Fe₃C–carbon composites as seen in PXRD results of T-MIL-88B-500 and T-MIL-88B-505, respectively (Fig. 1c and Fig. S1c). For N₂ environment, no derivative weight loss peak was observed between 495–565 °C. However, a sharp peak was detected between 565–650 °C which might be due to the formation of Fe⁰–carbon composite reported in the literature for MIL-88B treatment at 600 °C and 700 °C under N₂ atmosphere³⁷. Overall, the weight loss of MIL-88B under 5%H₂/N₂ gas mixture atmosphere (84.4%) is higher as compared to N₂ environment (79.7%).

Figure S5 (ESI) presents CO₂-TPD results of T-MIL-88B-500 catalyst to measure the basicity of the catalyst. The surface basic sites were categorized as weak (50–212 °C), medium (212–328 °C), and strong (328–458 °C) basicity. In addition to the support, iron oxide nanoparticles may also adsorb CO₂^{50,51}. Overall, total quantity of desorbed carbon dioxide was 16.29 μmol/g from T-MIL-88B-500, where, the amount of CO₂ desorbed from weak, medium and strong basic sites were 12.24, 1.92 and 2.13 μmol/g, respectively.

Role of Fe-based zeolite and MOF catalysts

Figure 5a–c illustrates the yield and selectivity of AA via aqueous phase CO₂ reduction with iodomethane at various pressures. All the catalysts showed some activity for AA production; however, T-MIL-88B-500 was clearly the most active and selective catalyst with the best yield of 504 mmol/g_{cat}·L and AA selectivity of 92.4%. Based on stoichiometric calculation, it is equivalent to 80.6% conversion of CH₃I into AA. Both Fe/CBEA and T-Fe/MIL-101 provide lower activity for CO₂ hydrogenation and >90% selectivity for FA production. With increasing pressure, the yield increased initially but the AA selectivity peaked at 60 bar for both Fe/CBEA and T-Fe/MIL-101. However, the AA yield and selectivity increases with increasing pressure for T-MIL-88B-500. Since Fe was present in the structural framework of T-MIL-88B-500, the thermally transformed catalyst consists of embedded active metal sites dispersed evenly in a carbon matrix³⁷. The high AA activity and the selectivity over T-MIL-88B-500 catalyst is most likely due to the presence of both Fe⁰ and Fe₃O₄ which assist the hydrogenation and C–C coupling reactions, respectively^{52,53}. Recently, Wang et al. reported the acetate production through formate (HCOO⁻) and carbene (CH₂) intermediate reaction pathway using hexagonal closed packed cobalt (HCP-Co) catalyst and NaOH additive which provided maximum 9.5% acetate yield after 6 h of reaction at 300 °C, 0.5 M NaOH, 40% water filling, and 40 mmol Co under 15 bar CO₂ and 35 bar H₂ atmosphere. However, the catalyst was inactive at lower temperature (<200 °C)³⁰. In comparison, this study shows 504 mmol/g_{cat}·L AA yield with 92.4% AA selectivity after 21 h of reaction over T-MIL-88B-500 at 150 °C, H₂/CO₂ = 1, CH₃I = 10 mmol, catalyst amount = 400 mg, H₂O = 40 mL and stirring speed = 200 RPM.

Extent of reaction with time

Figure 6a illustrates the extent of reaction over T-MIL-88B-500 to produce AA and FA via CO₂ hydrogenation with CH₃I as the starting material in the aqueous media. The reaction proceeds via formation of FA as the initial product, whereas AA was not detected until after 8 h of reaction. The AA yield and selectively sharply increased between 12 to

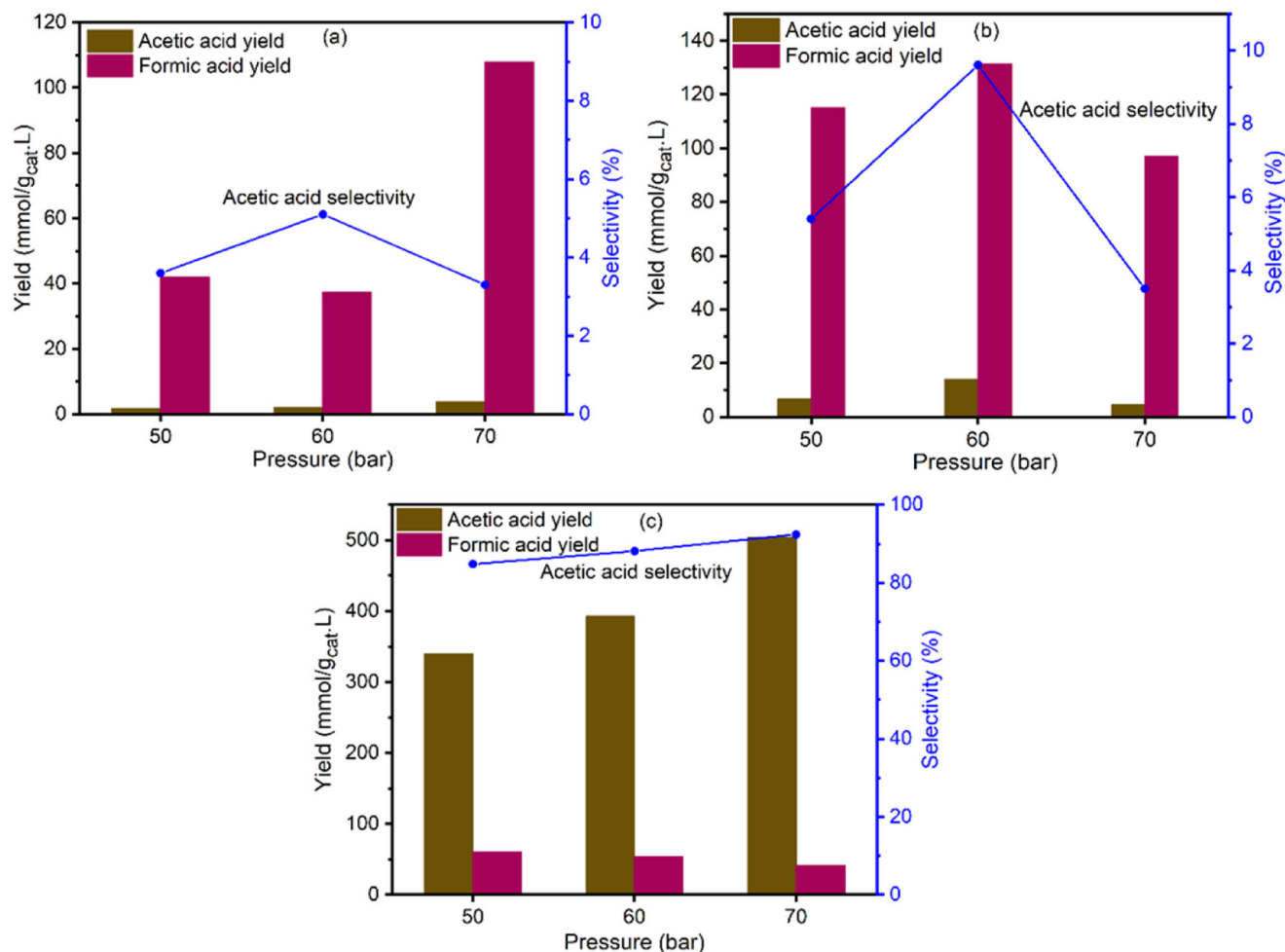


Fig. 5 | Yield and selectivity of formic and acetic acids produced on various Fe-based catalysts during aqueous phase CO₂ hydrogenation in the presence of CH₃I additive. a Fe/CBEA, b T-Fe/MIL-101, and c T-MIL-88B-500. Reaction

conditions: T = 150 °C, H₂/CO₂ = 1, t_R = 21 h, CH₃I = 10 mmol, amount of Fe/CBEA = 1 g, amount of T-Fe/MIL-101 = 400 mg, amount of T-MIL-88B-500 = 400 mg, H₂O = 40 mL and stirring speed = 200 RPM.

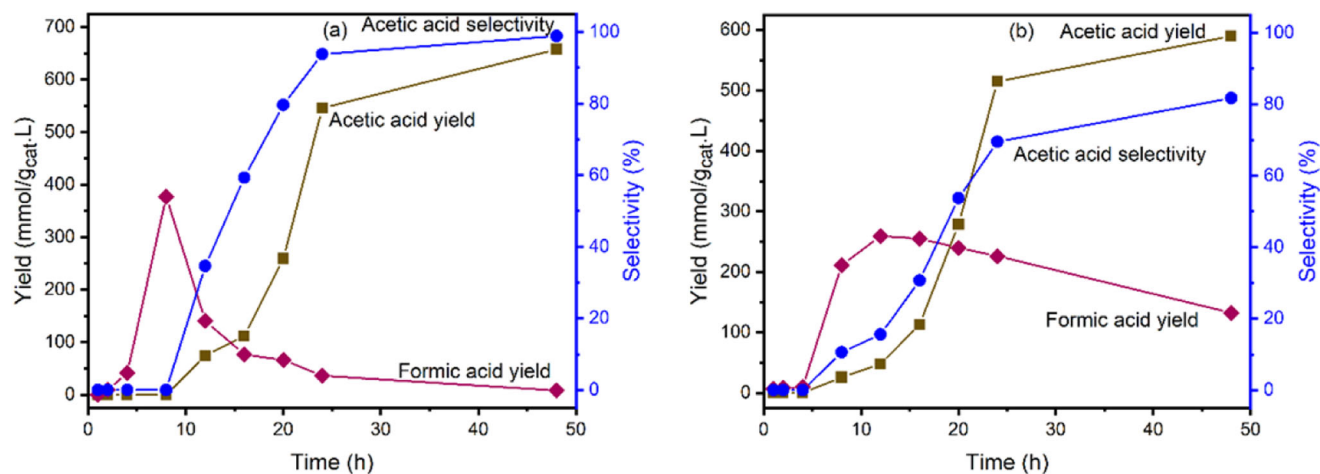


Fig. 6 | Effect of reaction time on carboxylic acids yield and selectivity via aqueous phase CO₂ hydrogenation over T-MIL-88B-500 in the presence of various additives. a CH₃I (10 mmol), and b CH₃OH (10 mmol) and Lil (10 mmol).

Reaction conditions: T = 150 °C, H₂/CO₂ = 1, catalyst amount = 400 mg, H₂O = 40 mL, P_{total} = 70 bar at room temperature and stirring speed = 200 RPM.

24 h, thereafter gradually increasing to 657.6 mmol/g_{cat}.L and 98.8%, respectively, at 48 h as the reaction approached equilibrium conversion. Based on the initial CH₃I concentration (10 mmol), 100% conversion at 100% selectivity for AA was achieved, within the range of

measurement errors. However, as discussed later, CO₂ first converts into FA and after reaching the maximum yield (377.4 mmol/g_{cat}.L) at 8 h, the FA yield decreases sharply until the end of reaction at 48 h when the FA yield was measured at 8.1 mmol/g_{cat}.L. However, since

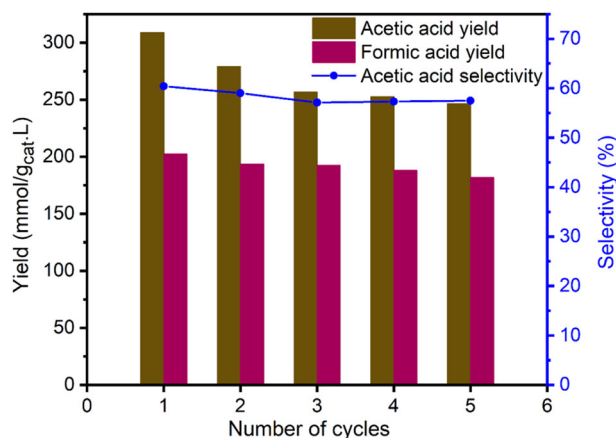


Fig. 7 | Recycling study of T-MIL-88B-500 via aqueous phase CO₂ hydrogenation in the presence of CH₃OH and Lil additives. Reaction conditions: T = 150 °C, H₂/CO₂ = 1, t_R = 21 h, CH₃OH = 10 mmol, Lil = 10 mmol, catalyst amount = 400 mg, H₂O = 40 mL, P_{total} = 70 bar at room temperature and stirring speed = 200 RPM.

CH₃I is consumed by this time, the residual FA cannot convert into AA. Therefore, for the CO₂ hydrogenated into carboxylic acids, the selectivity of AA is 98.8%.

When CH₃OH (10 mmol) was used as a reactant with Lil as a co-catalyst (Fig. 6b), in otherwise identical reaction conditions, the reaction generates in situ CH₃I and hence the peak of FA is broader than Fig. 6a. The AA yield and selectivity increased more gradually and achieved a similar yield of 590.1 mmol/g_{cat}.L at 81.7% selectivity after 48 h, which is equivalent to 94% conversion of CH₃OH into AA. The in situ production of CH₃I slowed down the conversion of FA into AA, which may be due to mass transfer limitation.

Catalyst reusability

Figure 7 shows that the catalytic activity dropped initially but after three cycles, there was no significant decline in AA yield and selectivity. The PXRD of the used catalyst after five cycles (Fig. 1c), and the TEM image (Fig. 4f) and PSD (Fig. 4h) of used catalyst after 48 h confirmed that the structure is stable and there was no sintering or agglomeration of Fe⁰ and Fe₃O₄ nanoparticles in T-MIL-88B-500. The initial loss in activity is likely due to the loss of small particles of the catalyst which could not be recollected in centrifuge.

Proposed reaction pathway

Reaction mechanism of hydrocarboxylation of methanol in an organic solvent proceeds via reaction of CH₃OH with Lil to produce CH₃I and LiOH which is similar to the carbonylation of methanol (Monsanto process) followed by formation of CH₃Rh*^I due to the oxidative addition of CH₃I into a Rh* complexing catalyst¹⁶. Further, CO₂ is inserted into CH₃-Rh bond to produce CH₃COORh*^I. Finally, CH₃COOH is formed via reduction of CH₃COORh*^I with H₂ molecule in the presence of Ru* to produce HI as an intermediate. Whereas, Lil is regenerated in situ via HI formation which reacts with LiOH to produce H₂O and Lil. However, here we show aqueous phase methanol hydrocarboxylation in which the reaction pathway deviates from the published works and FA is formed as an intermediate.

First, we show that FA can react with CH₃I in water over T-MIL-88B-500 in H₂ atmosphere (Fig. 8). The conversion of FA closely follows AA yield and after 24 h of the reaction FA conversion of 91.5% is achieved with 100% AA selectivity.

Next, we show aqueous phase hydrocarboxylation of CH₃OH using T-MIL-88B-500 as catalyst and Lil as co-catalyst. Here both liquid and gas samples were collected after 48 h of reaction. The liquid sample showed only the presence of HCOOH and CH₃COOH with 81.7% acetic acid selectivity (Fig. 6b). Whereas gas analysis did not detect any

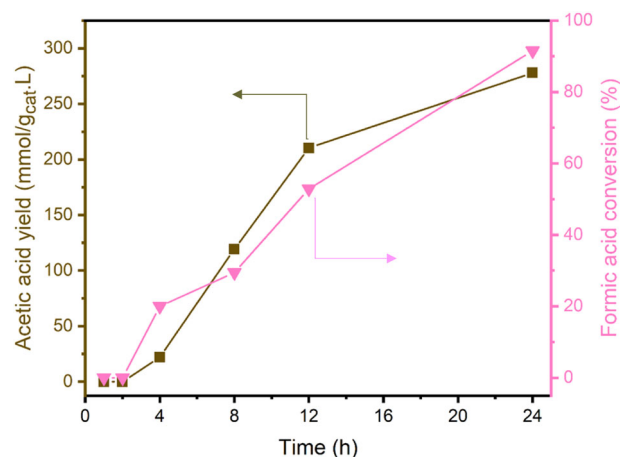


Fig. 8 | Acetic acid production through HCOOH and CH₃I reaction in water over T-MIL-88B-500 in the presence of hydrogen. Reaction conditions: T = 150 °C, catalyst amount = 400 mg, n_{HCOOH} = 5 mmol, n_{CH₃I} = 10 mmol, V_{H₂O} = 40 mL, P_{H₂} = 35 bar at room temperature and stirring speed = 200 RPM.

carbonaceous molecules apart from CO₂ (ESI, Fig. S8a, b), which eliminates the methanol carbonylation route for AA production.

Figure 9 shows the proposed reaction pathway for acetic acid production via hydrocarboxylation of CH₃OH over T-MIL-88B-500. CO₂ and H₂ adsorbed over the catalyst and converted into FA, which may desorb. Subsequently, the adsorbed formate species reacts with iodomethane (CH₃I) to allow C–C coupling reaction to take place which generates an acetate species and HI as the by-product. Finally, acetate species is converted into acetic acid, whilst Lil might be regenerated from LiOH and HI (step 8). The reaction mechanism of acetate production via formate (HCOO⁻) and CH₂ intermediates promotes acetate formation over hexagonal closed packed cobalt (HCP-Co) catalyst during CO₂ hydrogenation reaction³⁰. Additionally, Yatabe et al. described AA synthesis via CO₂ hydrogenation with CH₃I additive in aqueous phase using water-soluble Rh-based homogeneous catalyst via ¹³CH₃I isotopic labelling experiment to confirm the presence of ¹³CH₃COOH³¹.

In conclusion, we show that thermally transformed Fe-based metal organic framework-based catalyst (T-MIL-88B-500) exhibited high catalytic activity and stability for aqueous phase CO₂ transformation into acetic acid. Here, the catalytic activity and the structural property of T-MIL-88B-500 were compared with Fe/CBEA and thermally transformed Fe supported MIL-101 (T-Fe/MIL-101). The T-MIL-88B-500 consisted of both Fe⁰ and Fe₃O₄ phases, which catalyse hydrogenation and C–C coupling reactions, respectively, making this catalyst superior to the others tested here. We present an atomistic mechanism of MIL-88B thermal transformation by ReaxFF molecular dynamics simulations. First, the carboxylic group in the linker breaks to form CO and CO₂ forming Fe/FeOx clusters embedded in a carbonaceous matrix. At higher temperatures, metal oxide further reduces to Fe nanoparticles. The presence of sodium and other non-volatile impurities increases substantially in a thermally transformed MOF. The effect of such impurities on catalyst morphology may be explored in future research. In reaction experiments, CH₃OH, CO₂, and H₂ aqueous phase reactants and Lil promoter resulted in a maximum acetic acid yield of 590.1 mmol/g_{cat}.L, with 81.7% selectivity after 48 h at 150 °C. We propose that the hydrocarboxylation of methanol to make acetic acid is mediated by the formate route, which is evidenced by formic acid as an intermediate. The T-MIL-88B-500 catalyst was active for at least five cycles for acetic acid production without showing any signs of deactivation via sintering, oxidation, or phase change.

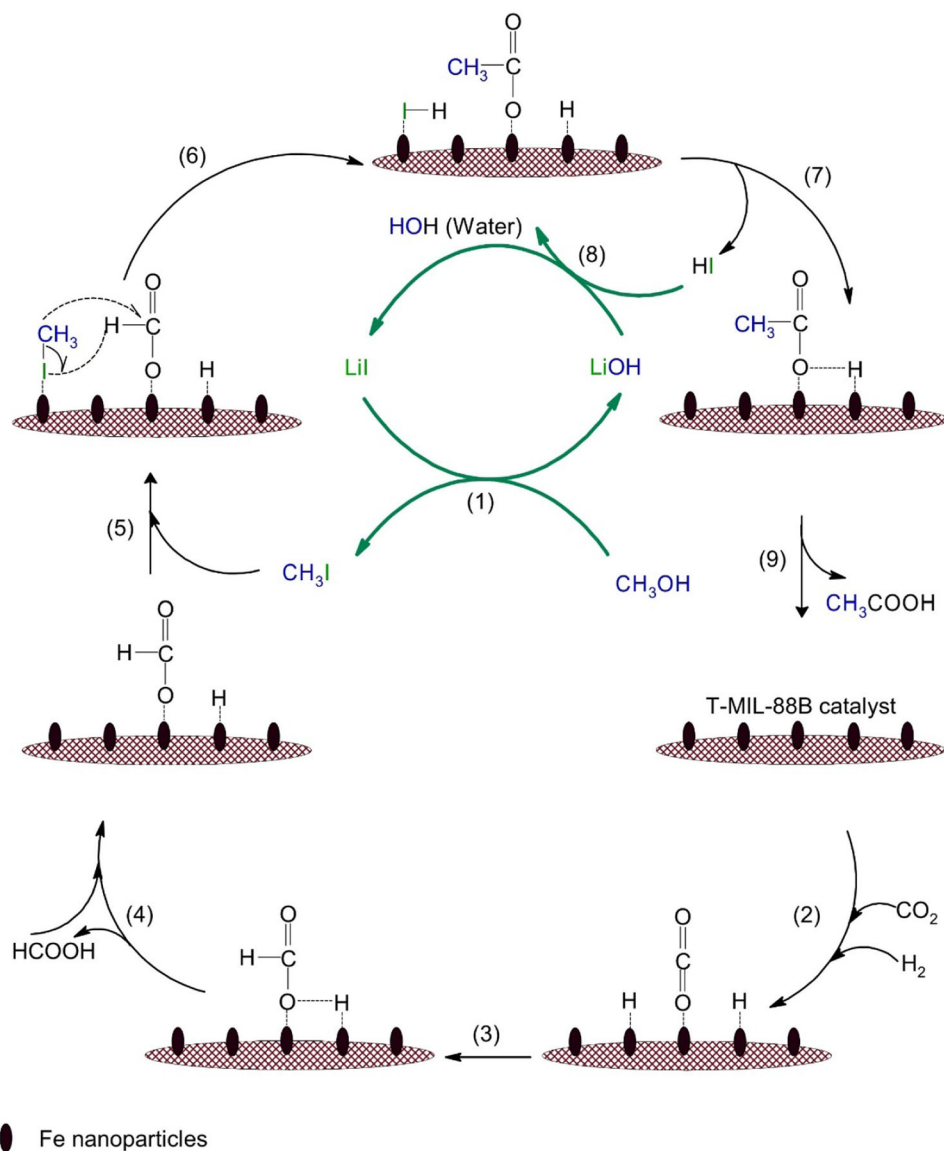


Fig. 9 | Possible reaction route for acetic acid production via aqueous phase CO_2 hydrogenation in the vicinity of methanol and LiI additives over T-MIL-88B-500 catalyst.

Methods

Materials

Iodomethane (CH_3I , 99.5%), formic acid (HCOOH , $\geq 95\%$), lithium iodide (LiI, 99.9%), terephthalic acid (H_2BDC , 98%), chromium chloride hexahydrate ($\text{CrCl}_3 \cdot 6\text{H}_2\text{O}$, 98%), and iron nitrate nonahydrate ($\text{Fe}(\text{NO}_3)_3 \cdot 9\text{H}_2\text{O}$, 98%) were purchased from the Sigma Aldrich. Commercial zeolite-beta (CBEA, $\text{SiO}_2/\text{Al}_2\text{O}_3 = 38$) was received from Zeolyst International. Methanol (HPLC grade) was obtained from the Scharlau Chemicals. Milli-Q water was used for catalysts synthesis (MIL-101 and Fe/CBEA) and acetic acid production experiments.

Catalysts synthesis

Wet impregnation process was used for Fe/CBEA synthesis as described in our previous publication¹¹. The loading of Fe was fixed as 10 wt% in this catalyst. Typically, $\text{Fe}(\text{NO}_3)_3 \cdot 9\text{H}_2\text{O}$ (7.2 g) was dissolved in Milli-Q water (30 mL) by using 100 mL Schott bottle and stirred for 15 min at 65 °C to prepare a homogeneous mixture of Fe solution. Thereafter, 9.0 g of CBEA support was immersed in this solution under stirring and maintained it for 6 h at the same temperature to achieve an even dispersion of Fe particles on CBEA support. The mixture was dried in oven at 100 °C followed by calcination at 550 °C with 5 °C/min for 5 h in

muffle furnace. Vertical tube furnace (50 cm length) and stainless steel (SS) reactor tube (length = 62 cm and outer diameter (OD) = 1/2 inch) were employed for reduction of catalyst. For this purpose, half of SS tube was firstly filled with quartz wool. Then, approximately 2 g of calcined Fe/CBEA catalyst was added in it and assembled in the SS reactor tube which was fitted to a homemade rig with gas controllers and tube furnace. The catalyst was reduced in the environment of H_2/Ar (1:1 v/v) gas mixture at 400 °C for 5 h with heating rate of 5 °C/min prior to carbon dioxide conversion experiment.

10 mmol of H_2BDC and 10 mmol $\text{CrCl}_3 \cdot 6\text{H}_2\text{O}$ were poured into a Teflon-lined autoclave. Subsequently, Milli-Q water (72 ml) was added to it. The reaction mixture was sonicated for 30 min followed by stirring for another 30 min at 500 rpm. Thereafter, the autoclave was kept in the oven at 205 °C for 24 h and allowed to cool to room temperature. The resulting solid suspension was transferred into a centrifuge tube. Initially, the centrifugation was performed at 138 relative centrifugal force (RCF) or g force for 3–4 min to remove the unreacted H_2BDC present in the reaction mixture. Thereafter, the centrifugation was carried out at 3444 g force for 10 min. The solid sample was then washed with dimethylformamide (DMF) three times and then dried in an oven at 70 °C for 12 h. The synthesised material was named as MIL-101.

For Fe/MIL-101 synthesis, 2.7 g of MIL-101 was suspended in 70 ml ethanol in a Schott bottle and sonicated for 30 min. Separately, 2.17 g $\text{Fe}(\text{NO}_3)_3 \cdot 9\text{H}_2\text{O}$ was dissolved in 20 ml ethanol in a different Schott bottle and stirred for 15 min. The latter solution was poured into the former suspension of MIL-101 in ethanol. Then the Schott bottle which contained $\text{Fe}(\text{NO}_3)_3$ solution was washed with 10 ml ethanol three times and poured into MIL-101 suspension each time to ensure complete transfer of the Fe precursor. The resultant mixture was sonicated for 30 min followed by stirring at 50 °C at 500 rpm for 5–6 h. Finally, the resulting reaction mixture was dried in an oven at 80 °C for 2–3 days. The synthesized catalyst was named as Fe/MIL-101. The Fe loading was fixed as 10 wt% in the synthesized catalyst. Prior to catalytic activity test, almost 2 g of this catalyst was thermally transformed under 100 ml/min H_2/Ar (1:1) gas mixture at 500 °C for 5 h with a heating rate of 5 °C/min and allowed to cool in 50 ml/min Ar atmosphere and denoted as T-Fe/MIL-101.

A modified hydrothermal method from literature³⁷ was adopted for synthesis of MIL-88B. In a typical procedure, 12.12 g of Fe salt ($\text{Fe}(\text{NO}_3)_3 \cdot 9\text{H}_2\text{O}$) was dissolved in 75 ml DMF under stirring (500 RPM) in a Schott bottle. Separately, H_2BDC (4.98 g) and DMF (75 ml) were added in a 250 ml Teflon-liner under stirring (500 RPM). Both Fe and H_2BDC solutions were stirred further for 15 min at room temperature. The Fe solution was then poured into H_2BDC precursor solution. 12 ml NaOH solution (4.0 M) was slowly transferred into Fe and H_2BDC solution mixture and stirred again for 30 min at room temperature. Thereafter, the Teflon-liner was sealed in an autoclave and heated to 100 °C for 24 h. After cooling to room temperature, MIL-88B particles were collected from this mixture via centrifugation at 6750 g force for 10 min and washed three times separately with DMF and methanol, respectively. Finally, the as synthesized MIL-88B was dried overnight in the oven at 80 °C and denoted as MIL-88B. Thermal transformation of MIL-88B was conducted in an identical vertical tube furnace attached with SS reactor tube as described before. 2 g of MIL-88B was thermally transformed at 495 °C, 500 °C or 505 °C for 5 h with a ramp of 5 °C/min under 100 ml/min H_2/Ar (1:1 v/v) environment followed by cooling to room temperature under Ar at 50 ml/min atmosphere and denoted as T-MIL-88B-495, T-MIL-88B-500 and T-MIL-88B-505.

Catalyst characterisation

The crystal structure of the materials was investigated with Powder X-ray diffraction (PXRD) using a Rigaku MiniFlex. Prior to the analysis, Fe/CBEA, Fe/MIL-101, and MIL-88 were reduced or thermally transformed as described above. The powder catalysts were loaded in a zero-background sample holder and scanned between 2–80° 2 θ with 4°/min scan speed at 15 mA and 40 kV, except for MIL-88B which was performed at 0.25°/min scan speed. Baseline correction of MIL-88B XRD was performed with OriginPro 2018 software. Nitrogen physisorption analysis was conducted with Micromeritics 3Flex 3500 machine to find the type of adsorption isotherm, Brunauer-Emmett-Teller (BET) surface area and Barrett-Joyner-Halenda (BJH) pore distribution. Tecani T20 was used to capture the transmission electron microscopy (TEM) images of the catalysts. All the samples were dispersed in ethanol and immobilised onto the surface of a holy carbon grid followed by drying in air prior to analysis. ThermoScientific K-Alpha machine was utilized for X-ray photoelectron spectroscopy (XPS) at 1486.6 eV E photon and coupled with monochromatic Al K α radiations. The binding energy (B.E.) baseline correction was conducted by adjusting the C 1s peaks at 284.8 eV. Thermally transformed samples were prepared ex situ prior to the XPS characterization. Fe L_{2,3}-edge X-ray absorption near edge structure (XANES) study of MIL-88B and T-MIL-88B samples were conducted in the Advanced Light Source, Lawrence Berkeley National Laboratory, in the Soft X-ray beamline 7.3.1. An energy range from 700 eV to 735 eV was measured at the end-station with a total pressure of 2.1×10^{-8} Torr using a 500 mA

ring current with 0.1 eV increments and 5 s count time. The XANES data were collected using total electron yield (TEY) mode, which measures the sample drain current as a result of photo and Auger electrons leaving the sample surface. Shimadzu DTG-60H thermogravimetric analyser was used to check the thermal stability of Fe/MIL-101 and MIL-88B. Both samples were analysed in the temperature range of 100–800 °C with a ramp of 5 °C/min under Ar atmosphere. MIL-88B thermal stability was evaluated in TA SDT 650 thermal analyser. 5 mg of MIL-88B sample was placed in an alumina pan and heated from room temperature to 800 °C with 5 °C/min heating rate under 100 mL/min 5%(v/v) H_2/N_2 gas mixture and ultra-high purity N_2 atmosphere. The surface basic sites of T-MIL-88B-500 were measured with carbon dioxide temperature programmed desorption (CO_2 -TPD) technique in a Micromeritics AutoChem II. Approximately 500 mg catalyst was preheated at 500 °C with 20 °C/min heating rate and kept at this temperature for 30 min, followed by cooling to 50 °C. Thereafter, 10% (v/v) CO_2/He gas mixture was passed through sample at 50 ml/min for 60 min, followed by He (50 ml/min) as a purge gas for 30 min before doing the CO_2 -TPD analysis between 50–500 °C at 10 °C/min heating rate under He flow. OriginPro 2018 software was chosen for baseline correction. CO pulse chemisorption was conducted (Micromeritics AutoChem II) to estimate Fe dispersion in T-MIL-88B-500 samples. Approximately 500 mg of sample was loaded in the sample tube and pretreated under 10% H_2/Ar gas mixture (50 ml/min) for 30 min at 500 °C with 10 °C/min. and purged with He (50 ml/min) for 30 min, followed by cooling to ambient temperature. Subsequently, it was heated to 35 °C at 5 °C/min and maintained at this temperature during the analysis, where, 10%(v/v) CO/He gas mixture (20 ml/min) and He (50 ml/min) gases were utilized as loop and carrier gases, respectively. Pulse gas injection was repeated 10 times at 6 min interval during this analysis.

Aqueous phase CO_2 conversion

All the aqueous phase CO_2 conversion experiments were performed in a 100 mL Teflon-lined autoclave batch reactor (Amar Equipment, M4). Typically, 400 mg of thermally transformed catalyst (T-MIL-88B-500) and 40 mL water was added to the reactor and CH_3I (10 mmol) was carefully poured into it and sealed. It was purged with H_2 three times to eliminate air from the headspace. The reactor was then pressurised with CO_2 up to 35 bar, followed by H_2 up to a total pressure of 70 bar at room temperature to achieve $\text{CO}_2:\text{H}_2$ ratio of 1:1. The reactor was heated to 150 °C under continuous stirring at 200 RPM for 21 h. After 21 h of reaction, the reactor was allowed to cool to room temperature and the remaining gases were carefully vented from it before disassembling it. The catalyst was recovered from the liquid product mixture by centrifugation at 9953 g force for 1 h. The same procedure was repeated for different total pressures at equimolar $\text{CO}_2:\text{H}_2$ ratio and different catalysts (T-Fe/MIL-101 and Fe/CBEA). Aqueous phase CO_2 transformation reaction was also performed at different time intervals employing the best catalyst to check the extent of reaction against time at 150 °C, equimolar $\text{CO}_2:\text{H}_2$ at 70 bar with 200 RPM stirring speed. The liquid samples were analysed using an HPLC (Agilent 1220 Infinity) equipped with a C18 column and a refractive index detector (RID), using 0.5 mM H_2SO_4 aqueous solution as the mobile phase. The product yields (mmol/g_{cat}·L) and selectivity (%) were calculated using Eqs. 6 and 7, respectively.

$$\text{Product}_i \text{ Yield} = \frac{n_i}{m_{\text{cat}} \cdot V_{\text{H}_2\text{O}}} \quad (6)$$

$$\text{Product selectivity} = \frac{n_i}{\sum_i n_i} \times 100 \quad (7)$$

Where n_i = moles of product, i = HCOOH or CH_3COOH , m_{cat} = mass of catalyst (g) and $V_{\text{H}_2\text{O}}$ = volume of water (L).

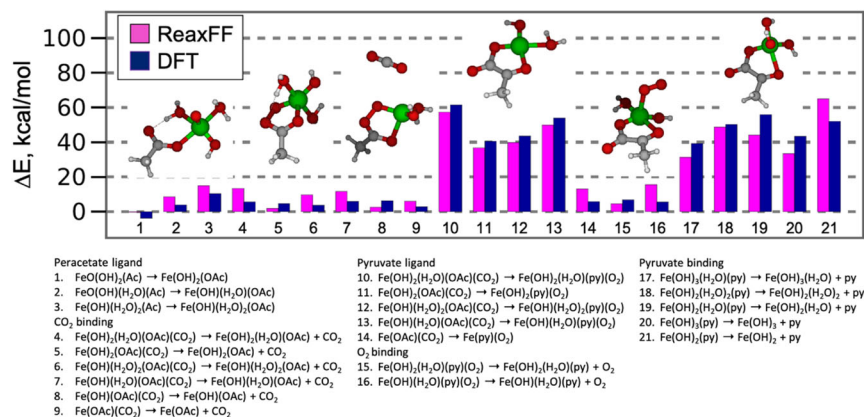


Fig. 10 | Comparison of ReaxFF and DFT for Fe(II)-complexes containing OH, H₂O, CO₂, O₂, acetate, peracetate and pyruvate ligands. Ac, OAc and py stand for

acetate anion, peracetate anion and pyruvate, respectively. Snapshots are Fe-complexes of acetate, peracetate, CO₂, pyruvate, O₂, and OH ligands, respectively.

The best catalyst was also evaluated for aqueous phase conversion using CO₂, H₂ and methanol (10 mmol) as reactants and lithium iodide (10 mmol) as the promoter. All other reaction conditions were identical to the previously described procedure.

Catalyst recycling study

The catalyst recyclability was investigated using CO₂, H₂ and CH₃OH (10 mmol) as reactants and LiI (10 mmol) as the promoter at 150 °C, equimolar H₂/CO₂ with 70 bar pressure at room temperature and 200 RPM stirring speed for 21 h in each cycle. After each cycle, the catalyst was recovered from the product mixture via centrifugation at 9953 g force for 1 h, and without any intermediate treatment, resuspended into a fresh reaction mixture at the same initial conditions. After five cycles, the centrifuged catalyst was dried overnight in oven at 70 °C and stored in an air tight glass vial for characterisation.

Reaction mechanism investigation

Reaction mechanism was explored by designing two different experiments—(1) using FA and CH₃I as reactants and experiment was conducted in water by using T-MIL-88B-500 catalyst at 150 °C under 35 bar hydrogen and 200 RPM stirring speed. Typically, 40 mL H₂O, 0.4 g of T-MIL-88B-500, 5 mmol (312.5 mmol/g_{cat}·L) of HCOOH and 10 mmol (625 mmol/g_{cat}·L) of CH₃I were added in Teflon-liner and reactor was sealed. After achieving the above-described conditions, 2 mL liquid sample was withdrawn from the reactor after regular intervals (1, 2, 4, 8, 12 and 24 h) for HPLC analysis. In the 2nd reaction system, aqueous phase CO₂ hydrogenation with CH₃OH (10 mmol) and LiI (10 mmol) was performed over T-MIL-88B-500 (0.4 g) for 48 h at 150 °C, 40 mL H₂O, equimolar H₂/CO₂ under 70 bar at room temperature and 200 RPM stirring speed. After 48 h, the reactor was cooled to room temperature. Both liquid and gas samples were collected for product analysis, where gas sample was analysed through Shimadzu 2014 GC coupled with TCD and FID detectors, respectively.

Computational methodology

The ReaxFF Fe/C/H/O force field employed in this work was originally developed to describe Fischer–Tropsch (FT) catalysis, and CO methanation and the hydrocarbon chain initiation^{54,55}. The force field had been trained for hydrogen adsorption, dissociation and migration on iron and iron carbide surfaces, and binding energies of small hydrocarbon radicals and energy barriers for CH₄ dissociation on Fe(100) surface. To extend this force field to describe MIL-88B model, Fe–O–C valence angle parameters were re-optimized against Fe-complexes relevant to the MIL-88B metal cluster topology. Figure 10 shows the energetics of mono- and bi-dentate Fe(II)-complexes containing OH, H₂O, CO₂, O₂, acetate, peracetate and pyruvate ligands,

which may appear in the catalytic iron coordination complex. The reaction energies for the conversion of acetate into peracetate, and peracetate into pyruvate are reproduced properly in ReaxFF. In addition, the binding energies of O₂, CO₂ and pyruvate ligand (strongest) to Fe(II) metal are in good agreement with the DFT data. A full description of this force field is given in Supplementary Data 1.

To mimic the thermal transformation of MIL-88B, we performed reactive molecular dynamics simulations using ReaxFF force field parameters. First, the MIL-88B(Fe) is equilibrated at 300 K under *NPT* ensemble for 100 ps. We use the Nose-Hoover thermostat and Berendsen barostat to control the temperature and pressure, respectively. To thermally transform the MOF, we keep the MOF at either 1500 K (200 ps and 500 ps) or 2000 K (500 ps) under *NVT* ensemble. Such high temperatures are commonly used in reactive molecular dynamics simulations to accelerate the reactions and mimic the experimental timescale (h) within computational timescale (ns). To reach these high temperatures, the MOF is heated at a rate of 2 K/ps under *NPT* ensemble below 1500 K and under *NVT* ensemble at 1500 K and above. The *NVT* ensemble is used for temperatures ≥ 1500 K to avoid an extremely low-density structure due to high temperature, which is not the case experimentally. Molecular dynamics is simulated with timestep of 0.25 fs (<1500 K) or 0.1 fs (>1500 K) and the damping constant for thermostat and barostat are 100 fs and 1500 fs, respectively. After 500 ps at high temperatures (1500 K and 2000 K), we cool the MOF to 300 K with a cooling rate of 4 K/ps. During cooling, we simulate *NPT* ensemble for $T < 1500$ K and *NVT* ensemble for $T \geq 1500$ K.

Data availability

All the data are available in the main text or the electronic supplementary information (ESI).

References

- Sattari, A., Ramazani, A., Aghahosseini, H. & Aroua, M. K. The application of polymer containing materials in CO₂ capturing via absorption and adsorption methods. *J. CO₂ Util.* **48**, 101526 (2021).
- Bahmanpour, A. M., Signorile, M. & Kröcher, O. Recent progress in syngas production via catalytic CO₂ hydrogenation reaction. *Appl. Catal. B: Environ.* **295**, 120319 (2021).
- Li, W. et al. A short review of recent advances in CO₂ hydrogenation to hydrocarbons over heterogeneous catalysts. *RSC Adv.* **8**, 7651–7669 (2018).
- Ahmad, W., Younis, M. N., Shawabkeh, R. & Ahmed, S. Synthesis of lanthanide series (La, Ce, Pr, Eu & Gd) promoted Ni/γ-Al₂O₃ catalysts for methanation of CO₂ at low temperature under atmospheric pressure. *Catal. Commun.* **100**, 121–126 (2017).

5. Ahmad, W., Al-Matar, A., Shawabkeh, R. & Rana, A. An experimental and thermodynamic study for conversion of CO₂ to CO and methane over Cu-K/Al₂O₃. *J. Environ. Chem. Eng.* **4**, 2725–2735 (2016).
6. Rui, N. et al. CO₂ hydrogenation to methanol over Pd/In₂O₃: effects of Pd and oxygen vacancy. *Appl. Catal. B: Environ.* **218**, 488–497 (2017).
7. Lee, D. K., Kim, D. S. & Kim, S. W. Selective formation of formaldehyde from carbon dioxide and hydrogen over PtCu/SiO₂. *Appl. Organomet. Chem.* **15**, 148–150 (2001).
8. Chan, F. L., Altinkaya, G., Fung, N. & Tanksale, A. Low temperature hydrogenation of carbon dioxide into formaldehyde in liquid media. *Catal. Today* **309**, 242–247 (2018).
9. Frusteri, F., Cordaro, M., Cannilla, C. & Bonura, G. Multifunctionality of Cu–ZnO–ZrO₂/H-ZSM5 catalysts for the one-step CO₂-to-DME hydrogenation reaction. *Appl. Catal. B: Environ.* **162**, 57–65 (2015).
10. Gao, P. et al. Direct conversion of CO₂ into liquid fuels with high selectivity over a bifunctional catalyst. *Nat. Chem.* **9**, 1019–1024 (2017).
11. Ahmad, W., Chan, F. L., Hoadley, A., Wang, H. & Tanksale, A. Synthesis of oxymethylene dimethyl ethers (OMe) via methanol mediated COx hydrogenation over Ru/BEA catalysts. *Appl. Catal. B: Environ.* **269**, 118765 (2020).
12. Siebert, M., Krennrich, G., Seibicke, M., Siegle, A. F. & Trapp, O. Identifying high-performance catalytic conditions for carbon dioxide reduction to dimethoxymethane by multivariate modelling. *Chem. Sci.* **10**, 10466–10474 (2019).
13. Corral-Pérez, J. J. et al. Decisive role of perimeter sites in silica-supported Ag nanoparticles in selective hydrogenation of CO₂ to methyl formate in the presence of methanol. *J. Am. Chem. Soc.* **140**, 13884–13891 (2018).
14. Preti, D., Resta, C., Squarcialupi, S. & Fachinetti, G. Carbon dioxide hydrogenation to formic acid by using a heterogeneous gold catalyst. *Angew. Chem.* **123**, 12759–12762 (2011).
15. Rohmann, K. et al. Hydrogenation of CO₂ to formic acid with a highly active ruthenium acridophos complex in DMSO and DMSO/water. *Angew. Chem. Int. Ed.* **55**, 8966–8969 (2016).
16. Qian, Q., Zhang, J., Cui, M. & Han, B. Synthesis of acetic acid via methanol hydrocarboxylation with CO₂ and H₂. *Nat. Commun.* **7**, 1–7 (2016).
17. Hasan, S., Ahmad, K., Isahak, W., Masdar, M. & Jahim, J. Synthesis of low-cost catalyst NiO (111) for CO₂ hydrogenation into short-chain carboxylic acids. *Int. J. Hydrog. Energy* **45**, 22281–22290 (2020).
18. Pal, P. & Nayak, J. Acetic acid production and purification: critical review towards process intensification. *Sep. Purif. Rev.* **46**, 44–61 (2017).
19. Luyben, M. L. & Tyréus, B. D. An industrial design/control study for the vinyl acetate monomer process. *Comput. Chem. Eng.* **22**, 867–877 (1998).
20. Padmanabhan, N., Deshpande, P. & Kuloor, N. Catalytic cracking of acetic acid to acetic anhydride. *Ind. Eng. Chem. Process Des. Dev.* **7**, 511–516 (1968).
21. Sato, H., Uraki, Y., Kishimoto, T. & Sano, Y. New process for producing cellulose acetate from wood in concentrated acetic acid. *Cellulose* **10**, 397–404 (2003).
22. Brown, P. M., Marquering, M. & Myerson, A. S. Purification of terephthalic acid by crystal aging. *Ind. Eng. Chem. Res.* **29**, 2089–2093 (1990).
23. Yoneda, N., Kusano, S., Yasui, M., Pujado, P. & Wilcher, S. Recent advances in processes and catalysts for the production of acetic acid. *Appl. Catal. A: Gen.* **221**, 253–265 (2001).
24. Ndoye, B., Lebecque, S., Destain, J., Guiro, A. T. & Thonart, P. A new pilot plant scale acetifier designed for vinegar production in Sub-Saharan Africa. *Process Biochem.* **42**, 1561–1565 (2007).
25. Budiman, A. W. et al. Review of acetic acid synthesis from various feedstocks through different catalytic processes. *Catal. Surv. Asia* **20**, 173–193 (2016).
26. Sibi, M. G. et al. Synthesis of monocarboxylic acids via direct CO₂ conversion over Ni–Zn intermetallic catalysts. *ACS Catal.* **11**, 8382–8398 (2021).
27. Cui, M., Qian, Q., Zhang, J., Chen, C. & Han, B. Efficient synthesis of acetic acid via Rh catalyzed methanol hydrocarboxylation with CO₂ and H₂ under milder conditions. *Green. Chem.* **19**, 3558–3565 (2017).
28. Hasan S. et al. In *IOP Conference Series: Earth and Environmental Science* (IOP Publishing, 2019).
29. He, C., Tian, G., Liu, Z. & Feng, S. A mild hydrothermal route to fix carbon dioxide to simple carboxylic acids. *Org. Lett.* **12**, 649–651 (2010).
30. Wang, X. et al. In situ formed metal oxide/metal interface enhanced C–C coupling in CO₂ reduction into CH₃COOH over hexagonal closed-packed cobalt. *ACS Sustain. Chem. Eng.* **9**, 1203–1212 (2021).
31. Yatabe, T. et al. Synthesis of acetic acid from CO₂, CH₃I and H₂ using a water-soluble electron storage catalyst. *Chem. Commun.* **57**, 4772–4774 (2021).
32. Lippi, R. et al. Highly active catalyst for CO₂ methanation derived from a metal organic framework template. *J. Mater. Chem. A* **5**, 12990–12997 (2017).
33. Lippi, R. et al. Unveiling the structural transitions during activation of a CO₂ methanation catalyst RuO/ZrO₂ synthesised from a MOF precursor. *Catal. Today* **368**, 66–77 (2021).
34. Alqarni, D. S. et al. Ru-zirconia catalyst derived from MIL140C for carbon dioxide conversion to methane. *Catal. Today* **371**, 120–133 (2021).
35. Ma, M. et al. Iron-based metal–organic frameworks MIL-88B and NH₂-MIL-88B: high quality microwave synthesis and solvent-induced lattice “breathing”. *Cryst. Growth Des.* **13**, 2286–2291 (2013).
36. Hou, S. et al. Green synthesis and evaluation of an iron-based metal–organic framework MIL-88B for efficient decontamination of arsenate from water. *Dalton Trans.* **47**, 2222–2231 (2018).
37. Liu, J. et al. Fe-MOF-derived highly active catalysts for carbon dioxide hydrogenation to valuable hydrocarbons. *J. CO₂ Util.* **21**, 100–107 (2017).
38. Dwivedi, S. et al. Atomistic mechanisms of thermal transformation in a Zr-metal organic framework, MIL-140C. *J. Phys. Chem. Lett.* **12**, 177–184 (2021).
39. Sun, J. L., Liu, P. A., Wang, M. J. & Liu, J. P. Molecular dynamics simulations of melting iron nanoparticles with/without defects using a Reaxff reactive force field. *Sci. Rep.* **10**, 3408 (2020).
40. Zhao, M. et al. Metal–organic frameworks as selectivity regulators for hydrogenation reactions. *Nature* **539**, 76–80 (2016).
41. Ma, Z., Song, T., Yuan, Y. & Yang, Y. Synergistic catalysis on Fe–Nx sites and Fe nanoparticles for efficient synthesis of quinolines and quinazolinones via oxidative coupling of amines and aldehydes. *Chem. Sci.* **10**, 10283–10289 (2019).
42. Koley, P. et al. Leveraging Cu/CuFe₂O₄-catalyzed biomass-derived furfural hydrodeoxygenation: a nanoscale metal–organic-framework template is the prime key. *ACS Appl. Mater. Interfaces* **12**, 21682–21700 (2020).
43. Lee, H. et al. Liquid phase plasma synthesis of iron oxide nanoparticles on nitrogen-doped activated carbon resulting in nanocomposite for supercapacitor applications. *Nanomaterials* **8**, 190 (2018).
44. Madhuvilakku, R., Alagar, S., Mariappan, R. & Piraman, S. Green one-pot synthesis of flowers-like Fe₃O₄/rGO hybrid nanocomposites for effective electrochemical detection of riboflavin and low-cost supercapacitor applications. *Sens. Actuators B: Chem.* **253**, 879–892 (2017).

45. Huo, Q. et al. Preparation of a direct Z-scheme α -Fe₂O₃/MIL-101 (Cr) hybrid for degradation of carbamazepine under visible light irradiation. *Appl. Catal. B: Environ.* **255**, 117751 (2019).
46. Guo, L., Qin, S., Yang, B., Liang, D. & Qiao, L. Effect of hydrogen on semiconductive properties of passive film on ferrite and austenite phases in a duplex stainless steel. *Sci. Rep.* **7**, 1–6 (2017).
47. Fen-rong, L. et al. XPS study on the change of carbon-containing groups and sulfur transformation on coal surface. *J. Fuel Chem. Technol.* **39**, 81–84 (2011).
48. Kim, D. et al. Interface electronic structures of BaTiO₃@ X nanoparticles (X = γ -Fe₂O₃, Fe₃O₄, α -Fe₂O₃, and Fe) investigated by XAS and XMCD. *Phys. Rev. B* **79**, 033402 (2009).
49. Liu, Z., He, W., Zhang, Q., Shapour, H. & Bakhtari, M. F. Preparation of a GO/MIL-101 (Fe) composite for the removal of methyl orange from aqueous solution. *ACS Omega* **6**, 4597–4608 (2021).
50. Cano, L. A., Cagnoli, M. V., Bengoa, J. F. & Marchetti, S. G. SBA-15 modified by incorporation of alkali metals: effect of its structural changes on the catalytic properties of Fe/SBA-15 system in the Fischer–Tropsch synthesis. *Energy Technol.* **8**, 2000150 (2020).
51. Xu, L. et al. The promotions of MnO and K₂O to Fe/silicalite-2 catalyst for the production of light alkenes from CO₂ hydrogenation. *Appl. Catal. A: Gen.* **173**, 19–25 (1998).
52. Zhang, L., Chen, X., Peng, Z. & Liang, C. Chemoselective hydrogenation of cinnamaldehyde over MOFs-derived M₂Si@C (M = Fe, Co, Ni) silicides catalysts. *Mol. Catal.* **449**, 14–24 (2018).
53. Zeng, T. et al. Fe₃O₄ nanoparticles: a robust and magnetically recoverable catalyst for three-component coupling of aldehyde, alkyne and amine. *Green. Chem.* **12**, 570–573 (2010).
54. Zou, C. Y., van Duin, A. C. T. & Sorescu, D. C. Theoretical investigation of hydrogen adsorption and dissociation on iron and iron carbide surfaces using the ReaxFF reactive force field method. *Top. Catal.* **55**, 391–401 (2012).
55. Zou, C. Y. & Van Duin, A. Investigation of complex iron surface catalytic chemistry using the ReaxFF reactive force field method. *Jom* **64**, 1426–1437 (2012).

Acknowledgements

The authors would like to thank the Faculty of Engineering, Monash University for financial support under the Researcher Accelerator Grant 2019. The Advanced Light Source synchrotron access was funded by Australian Research Council Discovery International Award (DP170104017). The authors would also acknowledge Monash Centre for Electron Microscopy (MCEM) for providing the microscopic analysis facilities. A.T. and A.S. received financial support from the Institute for Catalysis, Hokkaido University as part of their Strategic Research Fellowship grant scheme. This study was supported by the Cooperative Research Program of Institute for Catalysis, Hokkaido University (Proposal no. 19A1005). This research was also supported in part by the

Monash eResearch Centre and eSolutions-Research Support Services through the use of the MonARCH HPC Cluster.

Author contributions

Conceptualization: W.A., P.K. and A.T.; methodology: W.A., P.K., S.D., Y.K.S., A.S. and A.T.; investigation: W.A., P.K., R.L., S.D., Y.K.S., A.C.T.v.D., A.S. and A.T.; visualization: W.A., P.K., S.D., R.L. and A.T.; funding acquisition: A.S. and A.T.; project administration: A.T.; supervision: A.C.T.v.D., A.S. and A.T.; writing: W.A., P.K., R.L., S.D., Y.K.S., A.C.T.v.D. and A.T. W.A. and P.K. have equal contributions.

Competing interests

The authors declare no competing interests.

Additional information

Supplementary information The online version contains supplementary material available at <https://doi.org/10.1038/s41467-023-38506-5>.

Correspondence and requests for materials should be addressed to Akshat Tanksale.

Peer review information *Nature Communications* thanks the anonymous reviewers for their contribution to the peer review of this work. A peer review file is available.

Reprints and permissions information is available at <http://www.nature.com/reprints>

Publisher's note Springer Nature remains neutral with regard to jurisdictional claims in published maps and institutional affiliations.

Open Access This article is licensed under a Creative Commons Attribution 4.0 International License, which permits use, sharing, adaptation, distribution and reproduction in any medium or format, as long as you give appropriate credit to the original author(s) and the source, provide a link to the Creative Commons license, and indicate if changes were made. The images or other third party material in this article are included in the article's Creative Commons license, unless indicated otherwise in a credit line to the material. If material is not included in the article's Creative Commons license and your intended use is not permitted by statutory regulation or exceeds the permitted use, you will need to obtain permission directly from the copyright holder. To view a copy of this license, visit <http://creativecommons.org/licenses/by/4.0/>.

© The Author(s) 2023